

Continent-sized anomalous zones with low seismic velocity at the base of Earth's mantle

Edward J. Garnero¹, Allen K. McNamara¹, and Sang-Heon D. Shim¹

¹School of Earth and Space Exploration, Arizona State University, Tempe AZ, USA 85287-6004

In this paper, we discuss large low velocity provinces (LLVPs) in Earth's lowermost mantle, explore their dynamics and possible composition, and consider evolutionary scenarios. The question of thermochemical piles as the origin to LLVPs is important, as it forms the foundation for our understanding of the thermal state of the mantle, the thermal and chemical evolution of Earth's interior, the dynamics and geochemical significance of mantle plumes, and link to the driving forces causing plate tectonics. This supplementary material presents additional figures to support discussions presented in the main text.

Supplementary Figure S1 presents a number of tomography models, and compares details of LLSVPs, in particular, for 30% of the core-mantle boundary's (CMB's) area. For each model, the specific shear velocity reduction which, when a contour is computed, surrounds 30% of the CMB's area, is determined (and listed to the left of the models in Figure S1). The similarity among models of the long wavelength character of LLSVPs is striking. However, when scale lengths smaller than LLSVP dimensions are considered, significant variability (differences) among models is present (right column, Figure S1). This is not unexpected, given that different models use different methods and data. Resolution from region to region is typically non-uniform in

the tomographic approach. For example, Earth's southern hemisphere is significantly more poorly sampled¹⁰¹.

Figure S3 shows the locations where forward modeling studies have mapped strong changes in V_s occurring over short lateral distances, such as < 100 km. These are considered “sharp” in comparison to smoothly varying tomographically derived velocities.

We consider a related comparison of the first 8 tomographic models of Figure S1. We compare the lowest shear velocities in each model that occupy a defined percent of the CMB's area, and then we count the number of models having those lowest velocities in $1^\circ \times 1^\circ$ cells (Figure S2). When mapping the 10% of the CMB's area containing the lowest velocities in tomography models (top panel in Figure S2), we find that these regions are generally correlated with the interior of 30% area LLSVPs (red contours in Figure S1), with some geographical differences. For greater area percentages of the CMB (e.g., 20, 30, 40, and 50% areas, the other panels in Figure S2), a larger area of similarity between models is present, but differences in the perimeters of the low velocities are readily apparent. These differences are highlighted for the 30% area LLSVPs in Figure 1c (in the main text). The vertical extent of LLSVP low velocities varies from model to model (in both forward and inverse modeling), and depends on assumptions of the velocity value associated with their margins. Though, analyses of the depth distribution of shear velocity heterogeneity (δV_s) over the bottom 1800 km of the mantle (averaged laterally in $4^\circ \times 4^\circ$ cells) show strong similarity between models in their geographic distribution of their high-versus-low velocity clusters over that depth range².

Lateral gradients in the shear velocity perturbation maps were computed. Gradients were measured by computing the change in shear velocity over different lateral distances (from 3 to 10 degrees, which at the CMB corresponds to ~182 km and ~607 km, respectively). We display the amplitude of the gradient field for 10 degree measurement length in Figure S5. The strongest gradients are most commonly associated with the margins of LLSVPs. This is consistent with abrupt changes in shear velocity at those locations (and the thermochemical pile hypothesis).

A time snapshot from the geodynamic calculations of Li et al. (2014) (ref. 19) is explored in Figure S6. Composition and temperature fields are shown for a calculation with distinct thermochemical pile material, former oceanic crust material, and background mantle material. The zoomed in panels show that crust can enter the piles and add to compositional complexities, and that the temperature variability within thermochemical piles can be strong, which might be an explanation for observed seismic heterogeneity within LLSVPs. While the details depend strongly on model assumptions, we expect a similar result – that thermal and potentially chemical heterogeneity can persist within thermochemical piles, especially over long time periods.

Additional References

101. Simmons, N. A., Forte, A., Boschi, L. & Grand, S. P. GyPSuM: a joint tomographic model of mantle density and seismic wave speeds. *J. Geophys. Res.* **115**, B12310 (2010).
102. Houser, C., Masters, G., Shearer, P. & Laske, G. Shear and compressional velocity models of the mantle from cluster analysis of long-period waveforms. *Geophys. J. Int.* **174**, 195–212 (2008).
103. Kustowski, B., Ekstrom, G. & Dziewonski, A. M. Anisotropic shear-wave velocity structure of the Earth's mantle: a global model. *J. Geophys. Res.* **113**, B06306 (2008).
104. Mégnin, C., & Romanowicz, B. The shear velocity structure of the mantle from the inversion of body, surface, and higher modes waveforms. *Geophys. J. Int.* **143**, 709–728 (2000).
105. Grand, S. P. Mantle shear wave tomography and the fate of subducted slabs. *Phil. Trans. R. Soc. Lond. A* **360**, 2475-2491 (2002).
106. Becker, T. W. & Boschi, L. A comparison of tomographic and geodynamic mantle models. *Geochem. Geophys. Geosyst.* **3**, 2001GC000168 (2002).
107. Bréger, L. & Romanowicz, B. Thermal and chemical 3D heterogeneity in D". *Science* **282**, 718-720 (1998).
108. Luo, S., Ni, S., & Helmberger, D. V. Evidence for a sharp lateral variation of velocity at the core–mantle boundary from multipathed PKPab. *Earth Planet. Sci. Lett.*, **189**, 155-164 (2001).
109. Ni, S., Tan, E., Gurnis, M. & Helmberger, D. V. Sharp Sides to the African Superplume. *Science* **296**, 1850-1852 (2002).
110. Ni, S. & Helmberger, D. V. Further constraints on the African superplume structure. *Phys. Earth Planet. Int.* **140**, 243-251 (2003).
111. Ni, S. & Helmberger, D. V. Ridge-like lower mantle structure beneath South Africa. *J. Geophys. Res.* **108**, 2094 (2003).
112. Ni, S. & Helmberger, D. V. Seismological constraints on the South African superplume: could be the oldest distinct structure on Earth. *Earth Planet. Sci. Lett.* **206**, 119-131 (2003).
113. Ni, S., Helmberger, D. V. & Tromp, J. Three-dimensional structure of the African superplume from waveform modeling. *Geophys. J. Int.* **161**, 283-294 (2005).
114. Wang, Y. & Wen, L. Mapping the geometry and geographic distribution of a very-low velocity province at the base of the Earth's mantle. *J. Geophys. Res.* **109**, B10305 (2004).
115. To, A., Romanowicz, B., Capdeville, Y. & N. Takeuchi. 3D effects of sharp boundaries at the borders of the African and Pacific Superplumes: Observation and modeling. *Earth Planet. Sci. Lett.* **233**, 137-153 (2005).
116. He, Y., Wen, L. & Zheng, T. Geographic boundary and shear wave velocity structure of the “Pacific anomaly” near the core–mantle boundary beneath western Pacific. *Earth Planet. Sci. Lett.* **244**, 302-314 (2006).
117. Ford, S. R., Garnero, E. J. & McNamara, A. K. A strong lateral shear velocity gradient and anisotropy heterogeneity in the lowermost mantle beneath the southern Pacific. *J. Geophys. Res.* **111**, 1-14 (2006).

118. Sun, D., Tan, E., Helmberger, D. V. & M. Gurnis. Seismological support for the metastable superplume model, sharp features, and phase changes within the lower mantle. *Proc. Natl. Acad. Sci.* **104**, 9151-9155 (2007).
119. Sun, D., Helmberger, D. V., Ni, S. & Bower, D. Direct measures of lateral velocity variation in the deep Earth. *J. Geophys. Res.* **114**, 1-18 (2009).
120. He, Y. & Wen, L. Structural features and shear-velocity structure of the “Pacific Anomaly”. *J. Geophys. Res.* **114**, B02309 (2009).

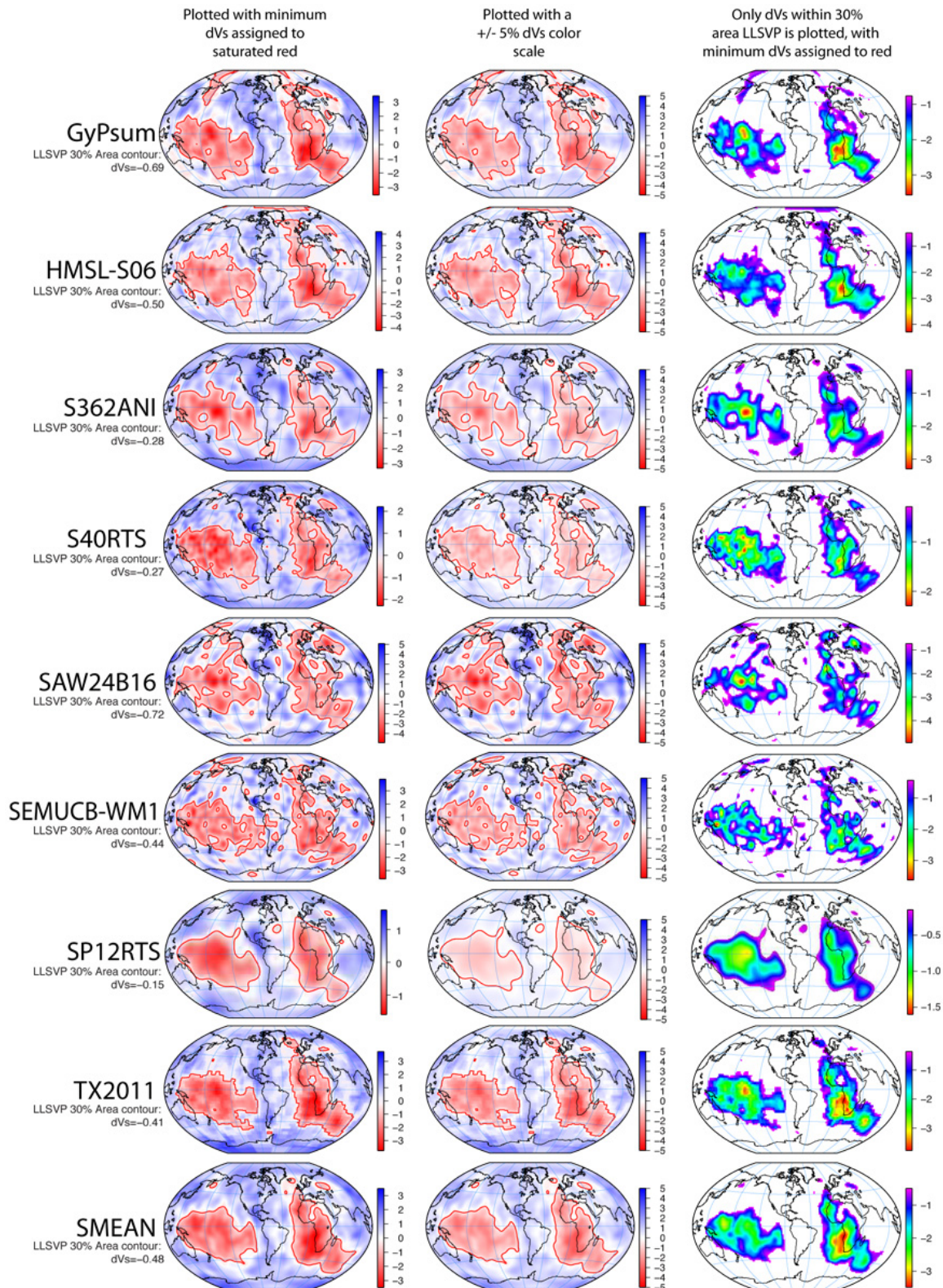


Figure S1 | Comparison of tomography model lowermost mantle velocities. (All scale bars in % δV_s). For 8 tomographic models (GyPsum (ref. 101), HML-S06 (ref. 102), S362ANI (ref. 103), S40RTS (ref. 1), SAW24B16 (ref. 104), SEMUCB-WM1 (ref. 8), SP12RTS (ref. 4), TX2011 (ref. 105)), and SMEAN, an average of models (ref. 106), the

lowest 200 km depth in each model is plotted. In the left column, the color scale extremes correspond to each model's extremes in high (blue) and low (red) shear velocity perturbations. A red contour is drawn at a velocity level for each model that surrounds 30% of the CMB containing the lowest shear velocities. Thus, the same CMB area (30%) is contoured for each model. The velocity reduction value that this corresponds to is shown on the left for each model. The middle column is the same as the left column, except the color scales are the same for all model renderings, and set at $\pm 5\%$, to show the amplitude differences between models. In the right column, only the area within the red contours of the left columns is considered (i.e., the 30% area LLSVPs), and the color scale is chosen to highlight shear velocity heterogeneity within LLSVPs for the CMB area coverage (again, 30%). The intermediate and small scale LLSVP heterogeneity differs from model to model.

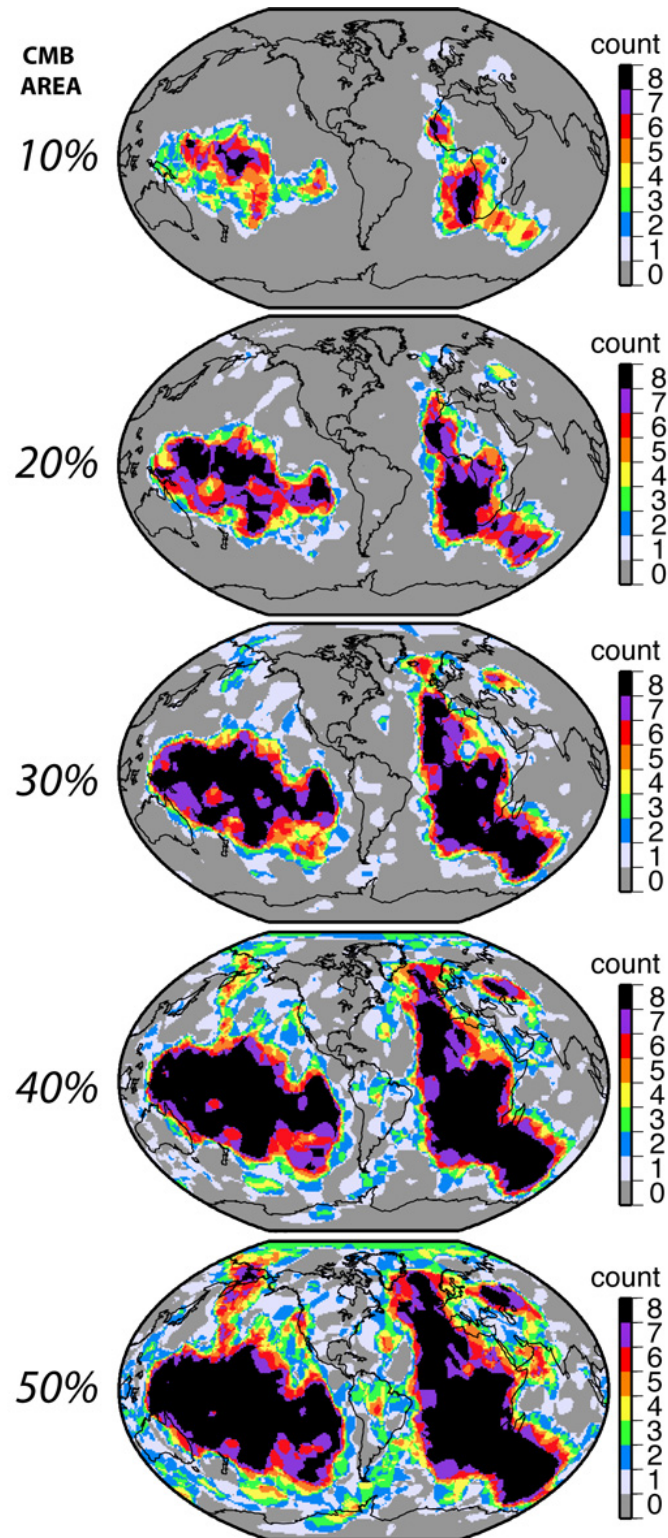


Figure S2 | Comparison of tomography model lowest velocity regions for specific CMB areas of coverage. For the first 8 tomographic models shown in Figure S1, the lowest velocities in each model are considered according to specific percentages of the area of the CMB. The CMB is gridded into $1^\circ \times 1^\circ$ cells, and models with lowest velocities

(for given CMB areas of consideration) are counted in all cells, and displayed in “vote maps”. Since 8 models are considered, a black color (as in the color scale) represents an area where all 8 models have some part of their lowest velocities at that location. Conversely, the color gray indicates that no model had its lowest velocities at that location, for the amount of LLSVP area considered. Five lowest velocity areas are considered 10, 20, 30, 40, and 50%.

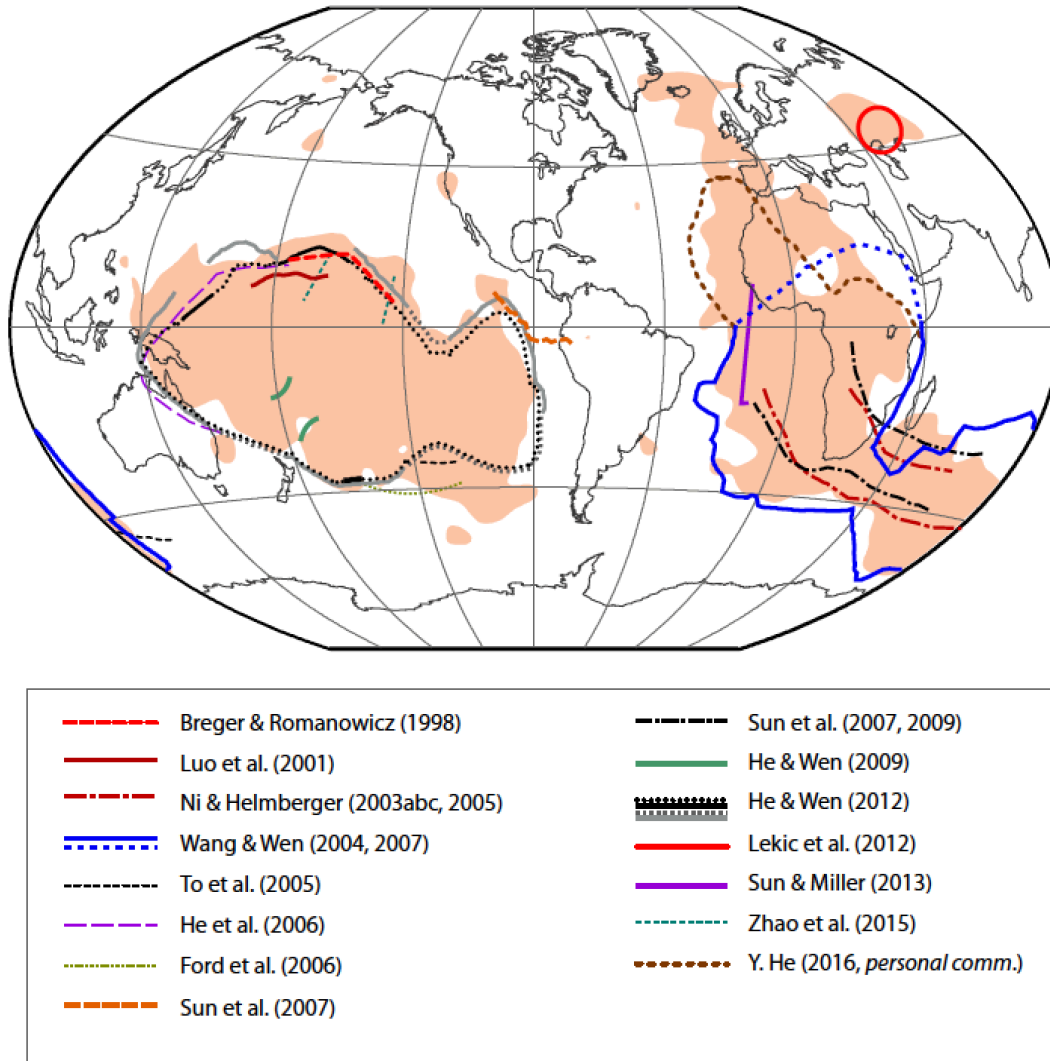


Figure S3 | Locations of sharp LLSVP edges. Waveform and travel time studies have presented evidence for sharp transitions in shear velocity at the margins of LLSVPs. The studies listed are Breger & Romanowicz (1998)¹⁰⁷, Luo et al. (2001)¹⁰⁸, Ni & Helmberger (2003abc) and Ni et al. (2002, 2005)¹⁰⁹⁻¹¹², Wang & Wen (2004, 2007)^{24,114}, To et al. (2005)¹¹⁵, He et al. (2006)¹¹⁶, Ford et al. (2006)¹¹⁷, Sun et al. (2007, 2009)^{118,119}, He & Wen (2009,2012)^{5,120}, Lekic et al. (2012)², Sun & Miller (2013)¹⁰, Zhao et al. (2015)⁹, and Yumei He (2006, *personal comm.*).

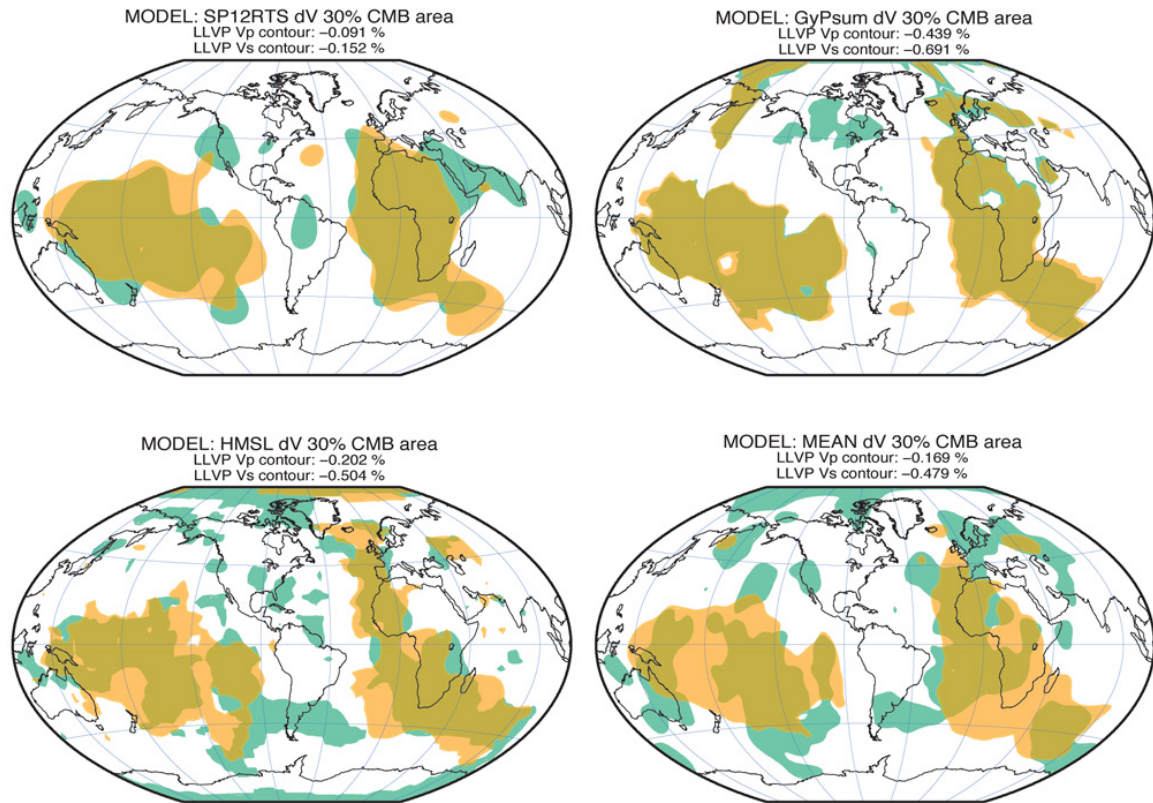


Figure S4 | Comparison of P-wave and S-wave LLVPs. The lowermost mantle velocity reductions for both P-wave (green) and S-wave (orange) LLVPs are displayed for 3 tomography studies that simultaneously inverted for Vp and Vs: SP12RTS (ref. 4), GyPsum (ref. 101), HMSL (ref. 102), and an average of P and S models, from PMEAN and SMEAN (ref. 106). LLVPs that occupy 30% of the CMB's area is displayed.

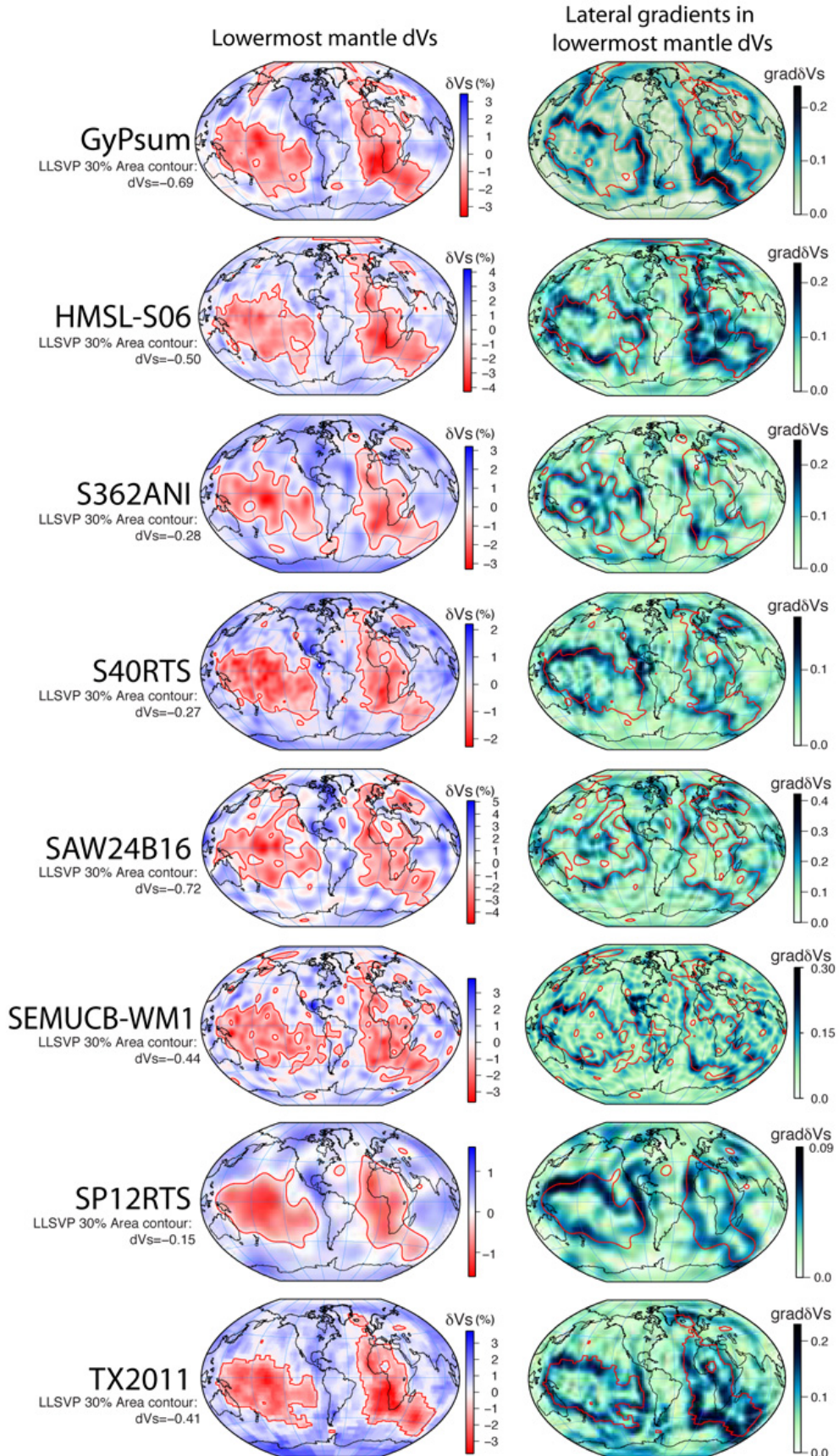
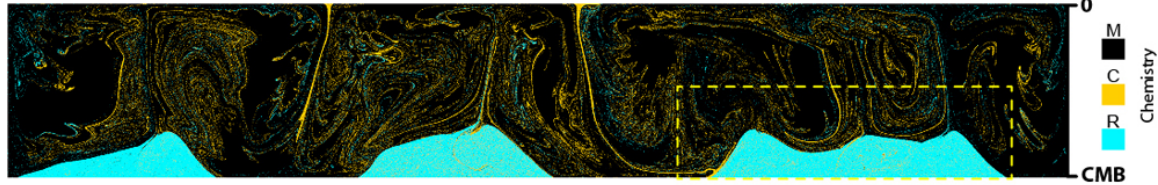
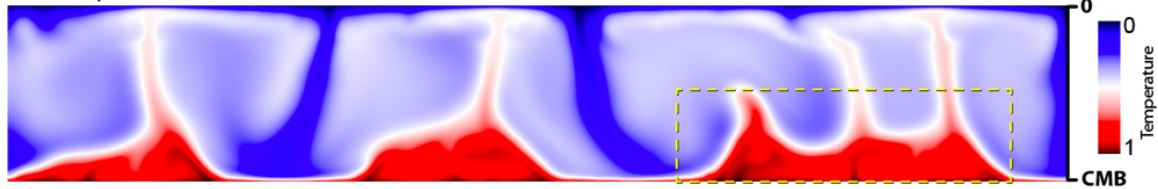


Figure S5 | Comparison of tomography model LLSVPs and strongest lateral gradients (previous page). *(Left column)* As with the left column in Figure S1, the shear velocity perturbations are shown in the lowest 200 km of the mantle, for 8 tomography models. The color scale is set for each model's extreme high or low shear velocities. The LLSVP contour is drawn for the 30% CMB area level. *(Right column)* Lateral gradients in the shear velocity perturbation field are plotted, where the darkest colors correspond to strongest gradients. The color scale for each model is different, and set by that model's maximum gradient. The LLSVP contour from the left column is reproduced on the gradient field, and shows the strongest gradients are commonly at the 30% area LLSVP margins. The maximum lateral gradient is computed over a 10 degree lateral length at every 1 deg by 1 deg location, which is plotted.

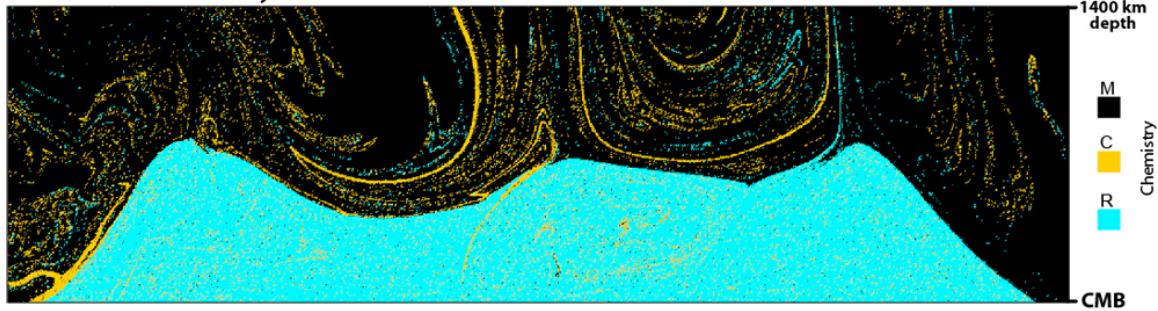
a Three chemistries: mantle, thermochemical piles, oceanic crust



b Temperature field



c Zoomed chemistry fields



d Zoomed, re-colored temperature field

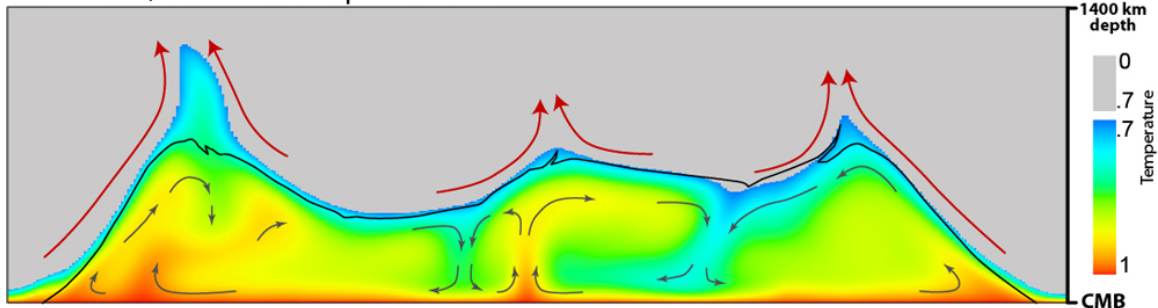


Figure S6 | Predictions of internal structure of thermochemical piles. From the calculations of Li et al. (2014)¹⁹ the dynamics, composition, and temperature are shown for a 3 chemistry system: a thermochemical reservoir at the base of the mantle (“R”), former basaltic oceanic crust (“C”), and background mantle (“M”). **a**, The compositional field is displayed for a time snapshot with thermochemical piles (turquoise color) well developed. Former oceanic crust (yellow color) is well mixed into the mantle (black color is the mantle), and has also been downward entrained into the piles. **b**, The temperature field for the time snapshot of **a** is shown. Panels **c** and **d** correspond to the zoom boxes in **a** and **b**, and show the composition and temperature. The temperature field in **d** is modified to show a complete color scale just within the thermochemical pile to highlight internal convection. The pile margin based on chemistry is indicated by the black line; flow directions are indicated by the arrows. For this example, the temperature field between .7 and 1 is colorized, with the rest plotted as gray.